NPL
National Physical Laboratory

NPL REPORT AC 14

A SCOPING STUDY OF THE POTENTIAL OF PHOTOACOUSTICS TO SUPPORT PRIMARY STANDARD CALIBRATION OF MEDICAL ULTRASONIC HYDROPHONES UP TO 100 MHz

SRINATH RAJAGOPAL
BAJRAM ZEQIRI
BEN COX

JULY 2015

National
Measurement
System

A Scoping Study of the Potential of Photoacoustics to Support Primary Standard Calibration of Medical Ultrasonic Hydrophones up to 100 MHz

Srinath Rajagopal
Bajram Zeqiri
Acoustics and Ionising Radiation Division, NPL

Ben Cox
Dept. Medical Physics and Bioengineering, University College London

ABSTRACT

Miniature medical hydrophone devices based on the piezo-electric effect, and hydrophones founded on fibre-optic Fabry-Perot interferometric principles are used to characterise the spatial and temporal properties of ultrasound fields. The quantity delivered by the hydrophone is an electrical waveform which can be transformed into the true acoustic waveform using a frequency dependent calibration factor with units of volts per pascal. Primary-level hydrophone calibration is carried out using an optical displacement interferometer. There is a pressing need to calibrate these hydrophones as high as 100 MHz due to an increasing proliferation of high frequency medical ultrasound scanners. However, calibration of these devices on the interferometer is extremely difficult at elevated frequencies due to the small, tens of picometre displacements generated by conventional mainstream ultrasound transducers. Environmental disturbances such as vibrations from seismic activity, movement of people in and around the laboratory and equipment cooling fans impose fundamental limitations on the smallest discernible displacements which can be measured, regardless of the type detection scheme used to build these extremely sensitive measurement instruments. Therefore, a viable alternative to support calibrations would be to boost the high frequency displacements, ideally to a few hundred picometres. Photoacoustics has a potential to do this. The photoacoustic effect refers to the phenomenon when a material illuminated with light absorbs photon energy, converting it into propagating acoustic waves within the material via one of several mechanisms. In principle, photoacoustics could be used to generate acoustic frequencies up to hundreds of gigahertz. Recently, photoacoustic sources made of nanocomposite materials have been able to generate planar ultrasound peak-positive pressure pulses as high as 12 MPa in the medical imaging frequency range. In order to understand the state of the art in photoacoustics research, a detailed literature review was conducted to establish its potential to support high frequency hydrophone calibration using the NPL primary standard displacement interferometer. In parallel with the review, a photoacoustic measurement facility was setup, with early measurements being conducted. The literature review findings and early experimental results have shown photoacoustics to be a promising new area of science for NPL offering the potential to tackle the challenge of high frequency primary standard calibration of hydrophones.

ISSN 1754-2936

National Physical Laboratory
Hampton Road, Teddington, Middlesex, TW11 0LW

Approved on behalf of NPLML by Dr Ian Severn, Head, Acoustics and Ionising Radiation Division.

CONTENTS

1 INTRODUCTION

In layman's terms ultrasound is largely known for the relative absence of bio-effects arising from human exposure when compared to electromagnetic radiation such as X-rays. This is true for medical ultrasound devices operating at diagnostic power levels and frequencies. But ultrasound can cause bio-effects and the safety of the technique is maintained by ensuring that exposure conditions are within the recognised safe limits. Ultrasound loses energy along its propagation path, with absorption leading to a temperature rise which is dependent on the power contained within the ultrasound beam and frequency (as loss increases with frequency). Also, lower frequency and high amplitude negative pressures can induce tissue mechanical damage via cavitation (Leighton 1994). These two effects are described by internationally agreed exposure parameters known as the Thermal Index (TI) and Mechanical Index (MI) (IEC62359 2010). TI and MI provide a means of estimating any potential bio-effect during diagnostic examination. The need to obtain an extensive set of qualitative and quantitative information from ultrasound scanners for improved diagnostic accuracy has resulted systems in employing higher frequencies (for improved resolution as low as 20 μm), higher acoustic pressure amplitude (for deep tissue penetration), long tone-bursts (for blood velocity estimates), injection of contrast agents in to blood stream (enhanced echogenicity for improved visualisation) and more lately temporally modulated ultrasound fields (for determining tissue mechanical properties). All these enhancements has meant that the potential for inducing bio-effects are relatively higher when compared to technology employed 20 years ago. Also, an intentional bio-effect can be applied for therapeutic benefits for treating soft tissue injuries or by elevating tissue ambient temperature within cancer therapy by creating thermal lesions in tissue (Szabo 2014).

Miniature medical ultrasonic hydrophones based on the piezo-electric effect and fibre-optic Fabry-Perot interferometric principles can be used to characterise the spatial and temporal properties of the applied ultrasound field. Characterisation is carried out in a bath of water mainly because this forms a major constituent of human tissue but also for more practical reasons: it easy to source, reproducible, can be reused and discarded. The measured quantity from a hydrophone of interest is the electrical representation of spatially sampled ultrasound pressure field related by a frequency dependant factor (frequency response or calibration) with units of volts per pascal, V Pa^{-1}. The accuracy of the sampled ultrasound is dependent on a knowledge of the calibration over a sufficiently wide frequency range. In practice the ultrasound field is mostly non-planar and therefore to avoid spatial-averaging effects due to the finite size of the hydrophone, devices of smaller sensing dimensions are required; a requirement which progressively more difficult to meet with increasing frequency. Fibre-optic based hydrophones with active sensing diameter in the range 10 – 100 μm suitable to meet these demands have been developed (Morris et al. 2005, Gopinath Minasamudram et al. 2009). Deconvolution for the non-uniform response for the hydrophone can be used, in some circumstances, to recover the true acoustic

waveform from its electrical representation (Hurrell 2004). In the majority of applications the transducer used to generate the ultrasound is pulsed and the frequency content of the pulse covers a broad frequency range. There are currently diagnostic scanners operating at centre frequencies as high as 50 – 70 MHz with a –6dB bandwidth of 50 % (Szabo 2014, VisualSonics 2015, DermaScan 2015, ArcScan 2015). This simply means that any measurement device should have a known frequency response up to the sum of centre frequency and upper –6dB cut-off frequency for deconvolution. However, determining the frequency response of medical hydrophones to meet the current frequency range (potentially up to 150 MHz) of commercially available ultrasound scanners remains one of the most difficult challenges for the ultrasound metrology community.

1.1 CALIBRATION OF HYDROPHONES

Improved characterisation of the exposure parameters highlighted earlier requires measurement methods that yield lower uncertainties, thereby increasing the overall confidence in the measured parameter. There are a number of measurement methods available to determine the frequency response of a hydrophone (IEC62127-2 2013) but only optical methods based on interferometric principles are capable of approaching the high frequency range of medical ultrasound. Interferometers established at National Measurement Institutes (NMIs) around the world (Preston et al. 2003, Koch & Molkenstruck 1999, Matsuda et al. 2014) are based on the displacement sensing Michelson interferometer (homodyne). The basic operating principle of the National Physical Laboratory (NPL) Michelson interferometer is illustrated in Figure 1.

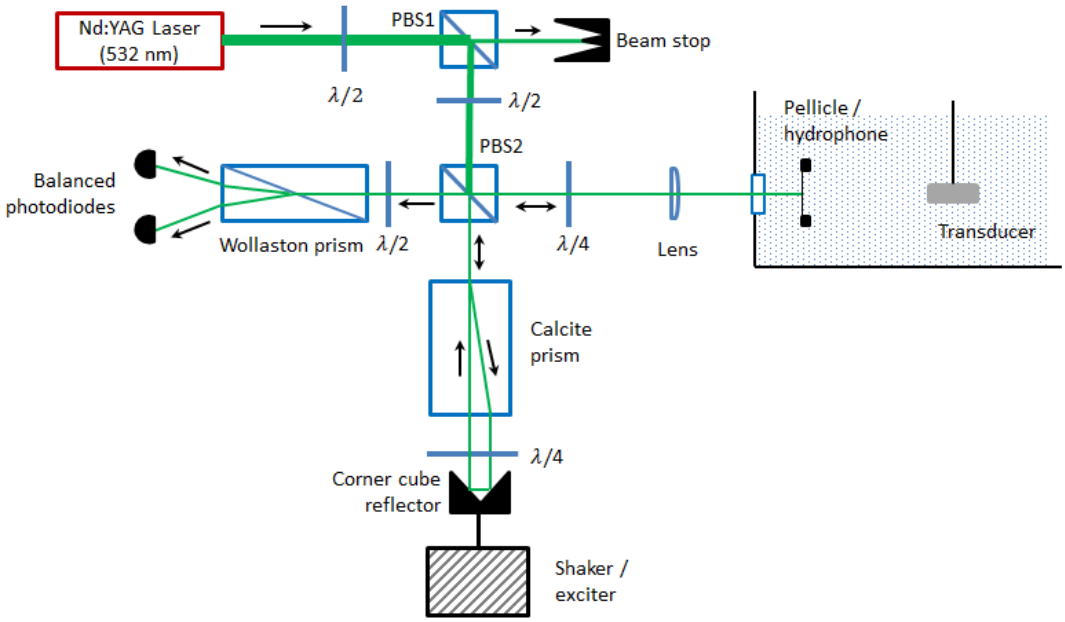

Figure 1 Schematic diagram of the NPL laser Michelson interferometer used for absolute displacement measurements at ultrasonic frequencies.

The measurement beam is illuminated on to a thin Mylar® pellicle (of thickness 5 μm) suspended in water and coated with a very thin layer of gold on the illumination side. The transducer exposes the pellicle to ultrasound from the opposite side. The thinness of the pellicle ensures it is acoustically transparent over the range of ultrasound frequencies of interest and it therefore follows the motion of sound in water. The reflected beam from the pellicle is combined with the reference beam and illuminated on to a pair of photodetectors configured in a balanced detector arrangement to minimise the influence of laser power fluctuations. The balanced photodetectors produce an electrical signal (V_I) by detecting the phase change between the stationary reference beam (i.e. fixed path length) and the measurement beam which has been disturbed by ultrasound propagation. The reference beam reflected off a corner-cube reflector mounted on a shaker (electromagnetic or piezo stack based) serves two functions: i) during the ultrasound displacement measurements, the shaker applies an instantaneous phase correction detected by the balanced photodetectors due to very low frequency (less than 1 kHz) mechanical disturbances caused by equipment cooling fans, air drafts and movement of operating personal in the lab. ii) produces a reference voltage (V_O) to convert the displacement signal V_I to absolute displacement in meters. The output of the Michelson interferometer, V_I, varies with displacement, a, according to the following relationship:

$$V_I = V_o \sin\left(\frac{4\pi\mu a}{\lambda} + \theta\right) \qquad (1)$$

where λ is the optical wavelength, V_O is the reference voltage corresponding to the amplitude of the output signal when the displacement exceeds λ/2, θ represents the phase shift between the measurement and reference optical beams and μ is the effective refractive index of the medium. For small ultrasonic amplitudes (less than 10 nm), the output can be assumed to vary linearly with displacement ($\sin(\theta) = \theta$ for small θ). Assuming plane-wave conditions, the acoustic pressure in the field may be calculated from the measured displacement by multiplying by the angular frequency, water density and speed of sound. The hydrophone is then substituted for the pellicle, with the acoustic centre placed in the field at exactly the same spatial location interrogated by the interferometer. The hydrophone output voltage, V_H, corresponding to this known acoustic pressure, is then measured, and the hydrophone sensitivity, M_H, derived using the expression:

$$M_H = \frac{V_H V_O}{V_I} \frac{2\mu}{\rho c f a} \qquad (2)$$

where f is the ultrasonic frequency, ρ and c are the density and speed of sound of water respectively at the particular temperature of interest. For absolute displacement measurements using optical

interferometry, the frequency response of the diode is also crucial as the photodetectors do not exhibit a flat amplitude response with frequency (Robinson et al. 1990, Koukoulas et al. 2013).

1.2 HIGH FREQUENCY CHALLENGE

Optical displacement interferometers based on homodyne principle are capable of resolving ultrasound displacements as small as tens of picometres. This kind of capability has enabled characterisation of hydrophones to frequencies as high as 60 to 70 MHz (Preston et al. 2003, Koch & Molkenstruck 1999) but this is not a trivial task and usually requires an exhaustive set of measurements to be undertaken each time a hydrophone is calibrated. Uncertainties associated with calibrations at these elevated frequencies are also significantly degraded. As a result, the user community has access to calibrations to a lower frequency of 40 MHz using dissemination methods on a routine basis (Koch 2003, Smith & Bacon 1990). Also, it is essential that laboratory infrastructure housing the interferometer is highly specified with regards to temperature control, scanning gantries being required for mapping spatial profiles of transducers, drafts due to any air conditioning units and more importantly the environment i.e. vibrations caused by seismic activity, movement of people in and around the laboratory, air-borne vibrations caused by cooling fans of amplifiers, oscilloscopes, computers and etc. A separate control-room could be used to house all the noise-generating equipment but most often this tends to be impractical and some processes cannot be automated to remove the user from the immediate vicinity of the measurement setup. Provided all this was under control, generating ultrasound plane-wave displacements of the order of 100 picometres and higher at frequencies as high as 100 MHz remains very challenging using main stream ultrasound transducer technology. The application of focused ultrasound transducers might be an option but the spatial beam-widths at higher frequencies tend to be only few hundred micrometres which means the uncertainty due to spatial-averaging effects can be significant resulting in excessive overall calibration uncertainty. For example the expanded uncertainty when using a focused transducer with known frequency dependant beam-widths to calibrate a hydrophone with a sensing diameter of 0.4 mm at 40 MHz is 6 %; at 100 MHz this is extrapolated to be 20 %. This is not ideal because the user hydrophone calibrated using dissemination methods will be likely to result in pressure measurement uncertainties in excess of 30 %. Therefore the confidence level in the determined exposure parameters is less likely to be useful or reliable.

1.3 PHOTOACOUSTICS

Photoacoustics could offer a solution to overcome limitations of existing ultrasound transducer technologies. The photoacoustic effect involves the generation of acoustic waves within a photosensitive material when it is illuminated with light. The material absorbs the photon energy and converts it into propagating acoustic waves via one of several intermediate processes such as

vaporisation, ablation, plasma formation, radiation pressure, surface melting, thermally-induced pressure rise, liquid fracture or cavitation, electrostriction, photo-dissociation and optical breakdown (Scruby and Drain 1990, Paltauf & Dyer 2003, Caddes 1966, Milas et al. 2003).

The photoacoustic effect was discovered in the late nineteenth century by Alexander Graham Bell, within a device he then termed a 'photophone', when he noticed that rapidly interrupted light incident on solid objects produced audible sound. It is only after the invention of laser in 1960 that the enormous potential of photoacoustic-related effects became realised and since then it has found widespread applications in many areas of science and engineering. For example, the wavelength dependant absorption of tissue in the visible and near infrared spectrum has led to the development of spectroscopic imaging of molecules and tissue that provide optical contrast with ultrasound imaging resolution (Wang 2009). The ability to excite acoustic waves with pulsed lasers and its detection using interferometric techniques through non-contact methods has been sufficiently exploited in non-destructive testing (NDT) of surface, sub-surface and deep-volume defects in materials as well as thin films (Huke et al. 2013, Zou et al. 2013). Recently an opto-acoustic microscope operating as high as 10 – 100 GHz has been developed for mapping single cell mechanics (Dehoux et al. 2015). Lately the use of carbon allotropes and plasmonic nano-particles has been exploited by many research groups in the development of efficient photoacoustic transducers for generating high amplitude broadband pressure sources for biomedical imaging. Summarising the results of a literature review, this report briefly discusses the theoretical background, highlights the developments in the field of photoacoustics and in particular the efforts to develop high frequency and high amplitude pressure waves. Finally the report provides recommendations on how to exploit this new area of science to support the calibration of medical ultrasonic hydrophones using the NPL primary standard interferometer, extended its upper working limit from the existing frequency of 40 MHz up to 100 MHz.

2 THEORY OF PHOTOACOUSTICS

2.1 PHOTOACOUSTIC WAVE GENERATION

There are a number of mechanisms that give rise to acoustic waves following light-matter interaction. However, the relevant mechanism employed in biomedical imaging and of importance within this report is that due to localised heating caused by a high energy pulsed laser inducing thermoelastic stresses and strains that acts as an ultrasonic source (Scruby and Drain 1990). The generation of ultrasound in the thermoelastic regime essentially involves three steps i) the absorption of a photon, ii) the thermalisation of absorbed energy and a corresponding localised increase in stress (compressive), and iii) the propagation of this stress as an acoustic wave due to the elastic nature of material (Cox 2009). Efficient photoacoustic wave generation requires satisfying two stringent conditions i.e. stress

relaxation ($t_s = d/c_0$) and thermal relaxation ($t_{th} = d^2/4\alpha_{th}$) times which must be much higher than the duration of the laser pulse, t_p (Cox 2009):

$$t_p \ll t_s \ll t_{th} \tag{3}$$

where d is the characteristic optical absorption length, c_0 is the speed of sound of the material and α_{th} is the thermal diffusivity of the material. The above time constraints ensures that inertia of the material has less time to react to the deposited thermal energy leading to build up of pressure within a fixed volume (isochoric) and consequently giving rise to the acoustic pressure amplitude characteristic of photoacoustics. This pressure rise is called the initial photoacoustic pressure distribution, p_0.

2.2 PHOTOACOUSTIC WAVE EQUATION

When considering the time duration of a laser pulse typical of those used in biomedical imaging frequencies (t_p = 1 – 10 ns), each of the processes i.e. photon absorption, thermalisation and propagation of acoustic wave happens in a sequential time scale. Therefore the heat source giving rise to the initial build-up of pressure can be assumed to be stationery ($t_p << t_{th}$). The other simplifying assumption is that the medium is inviscid. With this background the coupled photoacoustic wave equations i.e. wave equation for acoustic pressure (4) and diffusion equation for temperature (5) can be derived from first principles and in particular by using linearised mass, momentum, energy and entropy equations (Cox 2009, Diebold 2009):

$$\frac{\partial^2 p}{\partial t^2} - c_0^2 \nabla^2 p = \frac{\alpha}{\kappa_T} \frac{\partial^2 T}{\partial t^2}, \tag{4}$$

$$\frac{\partial T}{\partial t} - \nabla \cdot (D \nabla T) = \frac{H}{\rho_0 C_p}, \tag{5}$$

where p is the acoustic pressure, α is the volume thermal expansivity, κ_T is the isothermal bulk modulus (the reciprocal of compressibility), T is the temperature, $D = \kappa/\rho_0 C_p$ is the thermal diffusivity, ρ_0 is the mass density, κ is the thermal conductivity and H is the absorbed optical power density. If the thermal diffusion term in equation (5) can be neglected (based on thermal diffusion time scales) then equations (4) and (5) can be combined to give a single wave equation for pressure. The forcing function or the source term is the rate of change of absorbed optical power density:

$$\frac{1}{c_0^2} \frac{\partial^2 p}{\partial t^2} - \nabla^2 p = \frac{\alpha}{C_p} \frac{\partial H}{\partial t}, \tag{6}$$

Or equivalently

$$\left(\frac{\partial^2}{\partial t^2} - c_0^2\nabla^2\right)p = \Gamma\frac{\partial H}{\partial t}, \qquad (7)$$

where $\Gamma = \alpha c_0^2/C_p$ is the Grüneisen parameter, generally known as the conversion efficiency of absorbed energy to pressure. The absorbed optical power density is related to optical absorption coefficient μ_a, of the medium and optical fluence.

The stationary source term H can be decomposed into spatial and temporal components, $H(\mathbf{x}, t) = h_x(\mathbf{x})h_t(t)$, with the temporal shaping factor normalised such that, $\int_0^\infty h_t(t)dt = 1$, for convenience. If the duration of the heating pulse, t_p is less than the transit time of the sound across the characteristic length of the absorbing medium, d/c_0 which is the stress confinement criteria then the heat source can be approximated by a delta function, $h_t(t) \rightarrow \delta(t)$ as $T \rightarrow 0$. Therefore the source term in equation (7) becomes $\Gamma h_x\, \partial\delta/\partial t$ and solving equation (7) with this term is equivalent to solving the initial value problem

$$\left(\frac{\partial^2}{\partial t^2} - c_0^2\nabla^2\right)p = 0, \qquad (8)$$

with initial conditions

$$p|_{t=0} = \Gamma h_x \; and \frac{\partial p}{\partial t}|_{t=0} = 0. \qquad (9)$$

The second term in equation (9) is satisfied by a zero particle velocity.

2.3 SOLUTION TO A PHOTOACOUSTIC WAVE EQUATION

One possible solution to equation (7) in free-space can be obtained via Green's function method. Green's method provides the impulse response solution to the acoustic wave equation when the source term in equation (7) is replaced by a spatio-temporal Dirac delta impulse function of the form $-\delta(x)\delta(t)$. In one-dimension (1D) using Green's function method (Verweij et al. 2014) equation (7) is represented as follows:

$$\frac{\partial^2}{\partial x^2}G(x-x',t-t') - \frac{1}{c_0^2}\frac{\partial^2 G(x-x',t-t\prime)}{\partial t^2} = -\delta(x-x')\delta(t-t') \qquad (10)$$

On the right-hand side of the equation x' is the position and t' is the time instant of the spatio-temporal impulse point source.

The expression for the analytical solution of equation (10) is as follows:

$$G(x-x',t-t') = \frac{c_0}{2}\Pi\left(t-t'-\frac{|x-x'|}{c_0}\right) \qquad (11)$$

$G(x, t)$ is the Green's function and Π is the Heaviside step function.

The solution for pressure in equation (7) in 1D, $p(x, t)$ is then simply the convolution of Green's function solution with the source function integrated over x', the position and t', the time instant of the spatio-temporal heat source:

$$p(x,t) = \int_{x'}\int_{t'} \frac{c_0}{2}\Pi\left(t-t'-\frac{|x-x'|}{c_0}\right)\Gamma\frac{\partial H}{\partial t'}dx'dt' \qquad (11)$$

There exist a number of forward propagation models and Verweij et al. (2014) discusses the relative merits of each model for various problem domains.

3 LITERATURE REVIEW

3.1 GENERAL BACKGROUND

The use of photoacoustics spans a wide area of interest in science and engineering for example in NDT, material characterisation and microscopy. This section briefly summarises the efforts of several research groups who have attempted to use photoacoustics as an alternative for current ultrasound technologies for enhancing the existing biomedical applications and influencing future developments. The context of their research can be broadly categorised as follows:

a) Development of high resolution (20 µm or better) imaging utilising all optical ultrasound transmitter-receivers to overcome the disadvantages of piezoelectric and capacitive micro-machined ultrasound transducers (CMUTs).

b) Generation of unipolar pulses to aid controlled experiments for e.g. high resolution imaging, cavitation and to simplify wavelet decomposition of the received ultrasound signal in ultrasound modulated optical tomography.

c) Minimally invasive optical ultrasound transducers (fibre-optic based) for intravascular imaging and enable access to constrained spaces in NDT.

d) High frequency (> 15 MHz) and high pressure (tens of MPa) focused ultrasound as a tool for precision surgery and micro-scale fragmentation without the intervening effects of acoustic cavitation.

The optically absorbing material henceforth known as 'the target' in the reminder of the report can be realised using a number of different material types. The photoacoustic conversion efficiency is

dependent on the intrinsic properties of the chosen target i.e. the Grüneisen parameter, Γ. One way to control the amplitude is by varying the laser fluence but this is not always practical because higher laser fluence is likely to damage the target. Therefore in addition to controlling the laser fluence, tuning the target properties is the key to achieving high amplitude and high frequency photoacoustic pulse. Naturally available targets do not possess all the required properties and therefore most often targets are made of composite materials. This is in order to provide more control over the acoustic, optical and thermodynamic properties.

The base material/matrix of the composite is where the bulk acoustic wave is generated and usually composed of polymers such as para-Methoxy-N-methylamphetamine (PMMA), elastomeric material such as Polydimethylsiloxane (PDMS), epoxy resin, and generally those with high linear thermal expansion coefficient. This could be an assumption because materials with high linear thermal expansion coefficient gives to increased p_0. Optically absorbing materials are dispersed in to the matrix which absorb the light and convert it to heat; the heat is then transferred to the matrix leading to pressure rise and consequent propagation of acoustic wave within the matrix. Optically absorbing materials such as carbon black and graphite powder have been traditionally used. However, the need for high pressure and broad frequency photoacoustic pulse has encouraged researchers to investigate allotropes of carbon such as single walled carbon nanotubes (SWNTs), multi walled carbon nanotubes (MWNTs), carbon nanofibers (CNFs), graphene oxide (GO) – a single layer of graphite oxide and reduced graphene oxide (rGO) – closely resembling pristine graphene. Metamaterials (engineered materials such as plasmonic nanostructures) such as gold and silver nanoparticles (NPs) also have been investigated.

The optical and thermal properties of carbon allotropes and plasmonic nanoparticles are unique and are dependent on a number of parameters. For example SWNTs and MWNTs exist in different structural forms known as chiral vector – a parameter indicating how the graphene sheet is rolled to form a carbon nanotube, the diameter can range from 0.4 – 40 nm, length can vary from few micrometres to several millimetres resulting in a huge spread in their aspect ratio (length divided by diameter) and the presence of lattice defects (impurities) due to a particular synthesis technique employed (Spitalsky et al. 2010). Nevertheless, both SWNTs and MWNTs grown vertically as a dense forest have been shown to behave like a black body. The reflectance of a SWNT forest (300 – 500 μm height) studied by Mizuno et al. (2009) was found to be 0.01 – 0.02 over a spectral range of 0.2–2.0 μm and in case of MWNTs it is 0.01 over a spectral range of 2.5–15 μm (Theocharous et al. 2014). The transmitted light is trapped within the nanotube forest and eventually absorbed giving rise to heat. Interestingly, the heat transport capability of carbon nanotube forests is not efficient when compared to an isolated single/multi-walled carbon nanotube (S/MWNT). The literature values of measured thermal conductivity, κ collated in Lukes & Zhong (2007) of an isolated SWNT has a range of 300 –

10,000 W m^{-1} K^{-1} for tube length and diameter ranging from 1.4 – 3.6 µm and 1 – 28.2 nm respectively. The measured thermal conductivities of an isolated MWNT reported by Kim et al. (2001) and Li et al. (2009) are 3000 W m^{-1} K^{-1} and 1400 W m^{-1} K^{-1} respectively. These values are significantly low in the case of carbon nanotubes forest for example it is 50 W m^{-1} K^{-1} for lengths of 2 mm MWCNT sheet (Aliev et al 2009). When carbon nanotubes are dispersed in a polymer matrix the thermal conductivity increases only marginally. Hong et al. (2008) report that for a weight fraction of 1 – 4 % purified SWNT and MWNT in PMMA is approximately 2.5 – 1 W m^{-1} K^{-1} and 1.5 – 3.5 W m^{-1} K^{-1} respectively. Han and Fina (2011) in their review provide a comprehensive status of research in the thermal conductivity of carbon nanotubes and their polymer nanocomposites.

Metallic NPs such as gold (Au), silver (Ag) and platinum (Pt) absorb light via surface plasmon resonance mechanism. The oscillating electromagnetic field of the incoming light polarises the free surface electrons of the NPs with respect to their ionic core. This dipole oscillation along the direction of the electric field of the light reaches a maximum at a specific frequency, called surface plasmon resonance (SPR). This non-thermal electron distribution relaxes to the ground state by electron-electron scattering without losing the absorbed photon energy where electron temperature could reach as high as 1000 K. Further electron-phonon coupling and phonon-phonon interactions dissipate heat in to the surrounding medium (Link & El-Sayed 2000). Surface plasmon absorption is size dependant. Spherical NPs in the range 5 – 100 nm exhibit strong absorbance in the visible wavelength range of 500 – 600 nm whereas rods and cylindrical NPs exhibit resonances at multiple wavelengths depending on their aspect ratio. The increase in the aspect ratio of the nanorods leads to redshifts of the longitudinal SPR (El-Brolossy et al. 2008) giving some control over the absorption spectra.

3.2 FIBRE-OPTIC PHOTOACOUSTIC SOURCE

Biagi et al. (1997) were the first to realise a photoacoustic (PA) transducer using fibre-optics where they evaporated thin chromium (Cr) metal on a 600 µm core diameter fibre. They used a Q-switched Nd:YAG pulsed laser of 150 ns duration and 0.1 mJ energy. The centre frequency of the generated PA pulse was around 16 MHz with a –6 dB bandwidth of approximately 9 MHz. Only 3% absorption within the Cr film contributed to the PA pulse generation. This effort was followed up by coating the fibre-tip with optically efficient absorbing material such as graphite powder mixed with epoxy (Biagi et al. 2001). They employed a Q-switched Nd:YAG pulsed laser of 1064 nm wavelength, 6 ns pulse, 13 µJ energy and investigated the effect of film thickness on photoacoustic conversion efficiency. The optimisation resulted in large bandwidth PA pulse whose pressure amplitude was 20 kPa with a –3 dB bandwidth covering a 10 – 40 MHz range. The ultrasonic response was measured at a 2 mm distance from the fibre tip using a 50 MHz transducer (V3337; Panametrics Inc) calibrated using a PVDF membrane hydrophone (Marconi 699/1/00002/200). The work of Mosse et al. (2014) appears to

produce a 40 fold increase in pressure amplitude (0.81 MPa) when a 200 µm core diameter fibre was coated with CNT-PDMS composite when compared to Biagi et al. (1997). The laser employed was a Q-switched Nd:YAG pulsed laser of 1064 nm wavelength, 2 ns duration, and 11.4 µJ energy. The PA pulse was measured at 2 mm distance from the fibre tip using a 75 µm diameter PVDF probe hydrophone (Precision Acoustics Ltd). Vannacci et al. (2014) developed optoacoustic probes on optical fibre tips using Micro-Opto-Mechanical System (MOMS) technology. The target was designed by depositing a thin carbon film on the surface of a 100 µm silicon membrane which was later attached to the tip of optical fibre with core diameters of 200 µm and 600 µm respectively. The pulsed laser was a 532 nm wavelength Q-switched Nd:YAG, 0.5 ns duration and 50 µJ energy. The PA pulse was measured using a PVDF probe hydrophone (HGL-0200; Onda Corporation). The peak-to-peak pressure from 200 µm core fibre was 2.8 MPa at 0.5 mm distance from the source and the measureable frequency content extended to at least 150 MHz.

PA pulse generation has also been realised utilising SPR on various metallic structures deposited on the tip of an optical fibre. In case of Tian et al (2013), they deposited a 60 nm gold layer on a single and multi-mode optical fibre tips with core diameters of 8 µm and 62.5 µm respectively. They used focused ion beam to create a periodic array of nanopores of 80 nm with 130 nm spacing. The pulsed laser was 532 nm Nd:YAG with 5 ns duration and 3 µJ energy. The PA pulse amplitude was 2.73 kPa with a –3 dB bandwidth of 7 MHz. The ultrasonic response was measured at a 1.5 mm distance from the fibre tip using a PVDF probe hydrophone (HGL-0200; Onda Corporation). Gold nanocomposites made of Au NPs of 20 nm diameter dispersed in PDMS was applied on the tip of a 400 µm core diameter multi-mode fibre (Zou et al. 2014). The pulsed laser was 532 nm wavelength Q-switched Nd:YLF with 5 ns duration and 11 µJ energy. The PA pulse amplitude was 0.78 MPa with measureable frequency content extending up to at least 20 MHz when measured at 1.2 mm distance from the fibre tip using a PVDF probe hydrophone (HGL-0200; Onda Corporation). Theoretical studies have also been conducted to understand the PA generation mechanism and efficiency analysis using various photo absorbing materials on the surface of optical fibres (Wu Nan et al. 2010, Wang X et al. 2011, Sun K et al. 2011).

3.3 NON FIBRE-OPTIC PHOTOACOUSTIC SOURCE

Non fibre-optic PA sources were generally realised by coating the target on a transparent solid therefore the emitting area is much larger than optical-fibre core diameters discussed previously although both focussed and unfocussed illuminations were employed for specific applications. Buma et al. (2001) used a target made by spin coating cured mixture of PDMS, carbon black and toluene on to a microscope slide. The target was illuminated with a fibre amplified InGaAsP diode laser (1.55 µm) pulse of 10 ns duration and 30 nJ energy through a 5 cm focal length planoconvex

lens. They investigated the radiation pattern of the PA pulse in the frequency range 15 – 70 MHz as a potential PA array element alternative to piezo element. Later work suggested that the acoustic radiation spot size (10 µm) of the target was degraded by the leaky Rayleigh waves due to angular interrogation of the target (Buma T et al 2003). Hou et al. (2006a, 2006b) also exploited the high thermal expansion coefficient of PDMS for the high frequency generation of PA signal. They fabricated a target consisting of 2-D arrangement of gold nanoparticles, sandwiched between a transparent substrate and a 4.5 µm thick PDMS layer. This target when illuminated using a pulsed laser of 5 ns duration with 100 nJ energy to a spot size of 25 µm generated a PA pulse of 2 kPa amplitude at a distance of 10 mm. The same group fabricated a different target by depositing carbon black on a 11 µm thick PDMS and used 25 µJ energy which generated PA signal amplitude of 800 kPa at 10 mm distance with a –6 dB bandwidth of 80% centred at 60 MHz (Hou et al. 2007).

Won Baac et al. (2010) developed two targets, one was made by growing multi-walled CNTs on a fused silica substrate and then spin coating the PDMS and in another case a planar Au NP array was fabricated by using a metal transfer method on to the fused silica substrate. The targets were illuminated using pulsed laser of 6 ns duration and 3 mW cm^{-2} intensity. The optical beam diameter was approximately 20 mm and acoustic responses were measured using a 100 µm micro-ring resonator (Huang et al. 2008, Maxwell et al. 2008) situated at approximately 1.4 mm depicting a plane-wave generation-detection scheme. The measureable frequency content of the PA pulse of up to 120 MHz was observed. A 10 dB increase in amplitude was observed across the frequency spectrum for Au NP target when compared to a 100 nm thick Cr film and for CNT target it was 24 dB. A one dimensional photonic crystal-metallic (PCM) structure for high frequency photoacoustic generation was developed by Guo et al. (2011). The PCM was made of alternating multiple dielectric layers including a defect layer which bordered a metallic structure. The PCM operated in a total internal reflection geometry which absorbed about 90% of the incoming light of certain wavelength via SPR mechanism. The acoustic response was measured using a micro-ring resonator (Huang et al. 2008, Maxwell et al. 2008). The –6 dB bandwidth of the measured spectrum was 78 MHz and the amplitude of the PA signal was 28 kPa when measured at a distance of 10 mm.

Hwan Lee et al. (2012) and Park et al. (2013) investigated reduced graphene oxide (rGO) coated on thin aluminium film for high pressure and high frequency ultrasound using photoacoustics. They carried out a limited systematic study using 532 nm wavelength pulsed laser of 5 ns duration of varying energy densities on varying rGO thick coating on 100 nm aluminium film. They observed an acoustic pressure amplitude of approximately 9 MPa for a 100 nm thick rGO coated on a 100 nm thick aluminium film for a fluence of 56 mJ cm^{-2}. The PA pulse was measured using a HMB-0500 type calibrated membrane hydrophone (Onda Corporation) and had measureable frequency content up to 60 MHz. Very recently Hsieh et al. (2015) have made a target consisting of CNFs and PDMS. The

average diameter of CNFs employed was 132.7 nm from which a 24.4 um CNFs film was fabricated and spun coated with PDMS to give a final thickness of 57.9 µm. When this target was illuminated with a pulsed laser of 532 nm wavelength, 4 ns duration of 4.2 mJ energy they observed a maximum acoustic pressure of 12.15 MPa using a HGL-0085 type probe hydrophone (Onda Corporation) at a distance of 3.65 mm and contained measureable frequencies up to 50 MHz. A significant increase in pressure amplitudes was observed by converging the PA field using a CNT-PDMS lens (Baac et al. 2012). The acoustic pressure amplitude was in excess of 50 MPa and the spatial dimension of the acoustic field was 75 µm laterally and 400 µm axially. The PA signal had measureable frequencies up to 75 MHz.

3.4 OTHER RESEARCH OF INTEREST

PA signal amplification was observed for gold nano-rods coated with silica in aqueous solution (Chen et al. 2011). They measured the optical absorption spectra in the visible to near infrared region before and after coating the nanorods with silica to show that silica coating did not increase the absorbance and the signal amplification was due to changes in the interfacial heat resistance from gold to water due to the silica. In a related research Bayer et al. (2013) observed PA signal amplification when silica-coated nanoparticles (nanorods and nanospheres) were aggregated in comparison to dispersed nanoparticles suspended in deionised water. The aggregated and dispersed nanoparticles were of equal volume and the PA signal was measured for increasing nanoparticle concentration from approximately 0.5 to 3.5 $\times$ 10^{-11}. A seven fold increase in PA signal amplitude was observed in aggregated nanoparticle solution. The authors attributed this to a summation of overlapping thermal profiles within the solvent layer surrounding each individual nanoparticle. Similarly, reduced graphene oxide-coated AuNRs were also shown to amplify the PA signal (Moon et al. 2015).

Liu et al (2010) have shown PA signal enhancement by using a train of pulses where-in the duration of pulse train was smaller than the absorbing medium's stress and thermal relaxation times. Their aim was to improve the PA signal due to nonlinear optical absorption within endogenous molecules in tissue without using high intensity light thus avoiding potential tissue damage. The pulsed laser was 6 ps duration operating at 1064 nm with a repetition rate of 875 kHz. They showed that PA signal amplitude increased linearly with number of pulses and also examined the signal amplitude dependence on illumination energy and on two different optical absorption coefficients.

4 NPL PA MEASUREMENT PLATFORM

The initial data gathered from the experimental setup implemented at NPL which is at the early development stage has been interesting. The experimental setup at NPL (Figure 2) employs a Q-

Switched Nd:YAG laser (Litron Laser Ltd, Ruby, England) operating at 1064 nm whose pulse duration at full-width at half-maximum (FWHM) is 6 ns with a maximum energy of 130 mJ per pulse. The spatial profile of the laser is Gaussian shaped and nominally of 5 mm width which is put through a Galilean telescope of x5 magnification. The magnified laser beam is then converted to a homogenised illumination of 20 mm diameter using a plano-convex lens and a diffuser. The wide illumination ensures a plane-wave of sufficient dimension is excited compared to the active element of commercially available hydrophones thus eliminating spatial-averaging corrections during calibration. This beam is then illuminated on the target through an optical window of the transparent Perspex® water tank. In this arrangement the target is completely surrounded by the water. A 0.2 mm diameter broadband membrane hydrophone (Precision Acoustics Ltd, Dorchester, England) is supported on a 5-axis manual alignment control (x3 linear, x1 rotation and x1 tilt) to enable maximisation of the acoustic signal emitted by the target. The hydrophone was calibrated using NPL's secondary standard facility (Smith and Bacon 1990) up to 60 MHz for amplitude and phase. The measured signal from the hydrophone is acquired using a Tektronix DPO7254 (Beaverton, USA) oscilloscope.

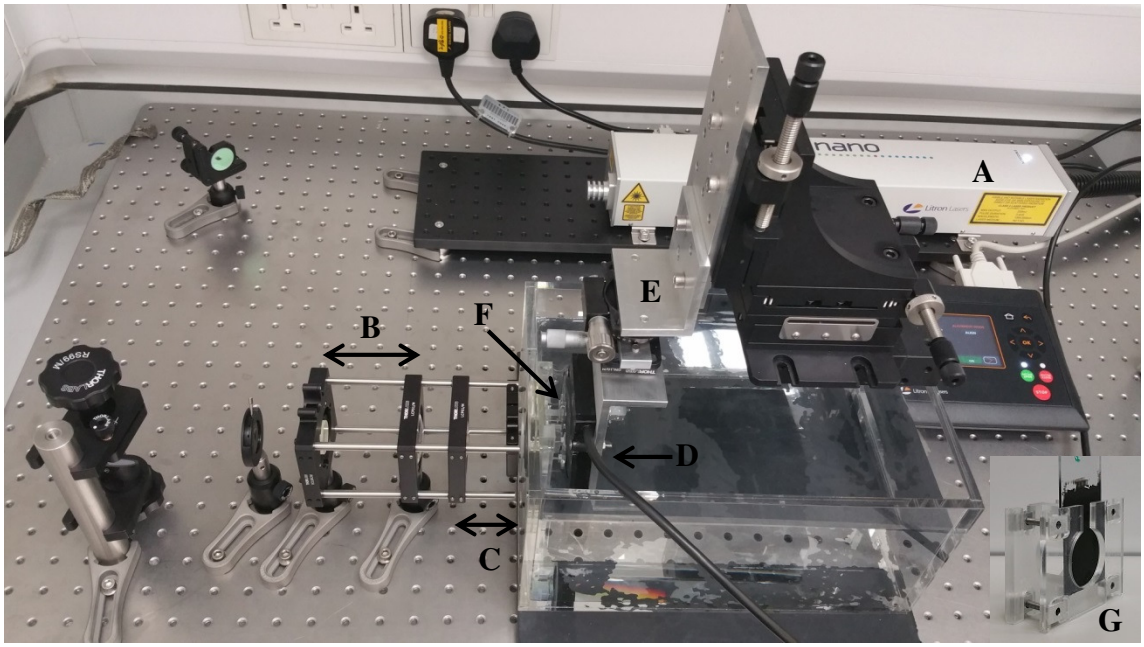

Figure 2 NPL Photoacoustic measurement setup. A – Laser; B – Galilean telescope; C – Beam homogeniser; D – Hydrophone, E – Hydrophone manipulator; F – Optical window; G – Target holder shown separately occupies a confined space in front of the optical window within the transparent Perspex® water tank.

The un-averaged single shot PA pulse (Figure 3) and its magnitude response (Figure 4) was obtained from a target realised by simply spray coating a layer of black paint of type PNM 400 (RS Components, UK) onto a laboratory glass slide. A total of 10 consecutive coatings were applied by rapidly stroking the sprayable paint which nearly completely blocked the visible light passing through

the layered paint-target. The laser was set to 100 % energy however, the actual energy impinging the target has not yet been fully quantified which needs to be implemented on the final NPL setup. The PA pulse duration determined from zero-crossing is approximately 47 ns. The magnitude spectrum has a dominant low frequency response with –6 dB bandwidth covering 0 – 30 MHz range.

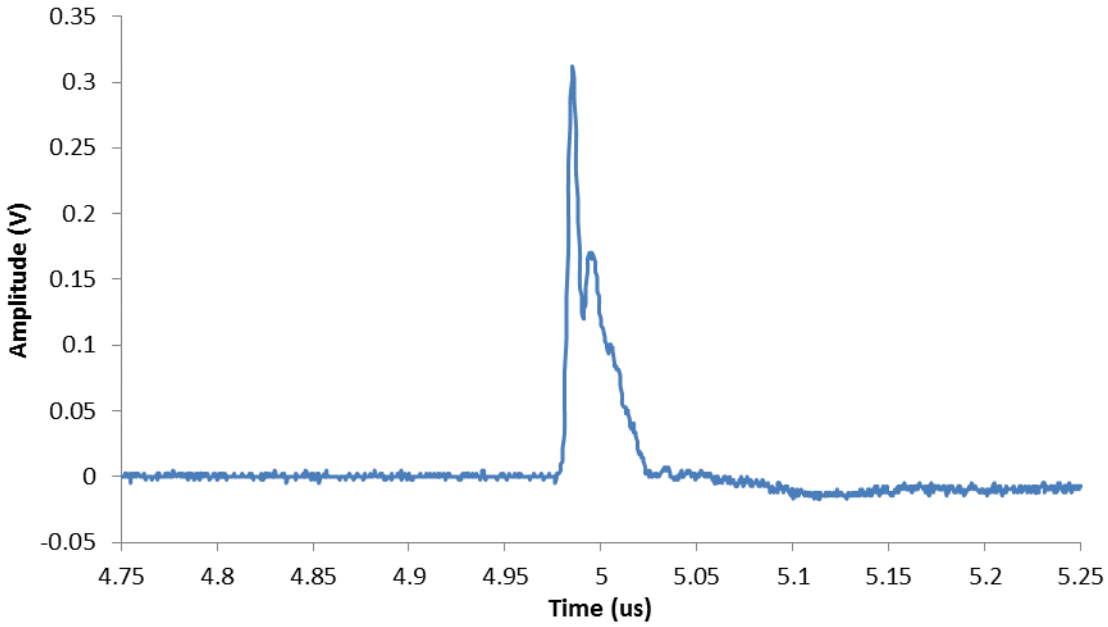

Figure 3 Photoacoustic pulse acquired at a distance of 7.5 mm from the target using a 0.2 mm diameter Precision Acoustics membrane hydrophone. The target was made from PNM 400 black spray paint coated on a glass slide and excited using a Q-switched laser operating at 1064 nm, 6 ns pulse duration and at 100 % energy.

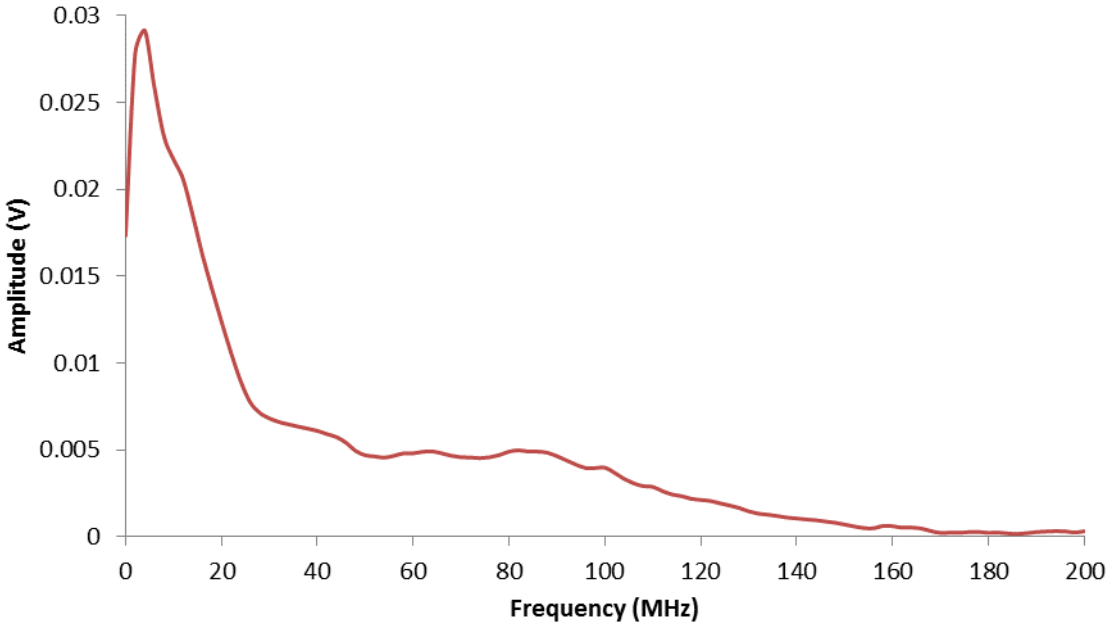

Figure 4 Magnitude spectrum of the PA pulse shown in Figure 3.

The PA pulse shown in Figure 3 was deconvolved (IEC62127-1 2013) using magnitude and phase response of the membrane hydrophone to a pressure pulse (Figure 5). The deconvolution process incurs significant errors since the PA pulse has frequency content up to at least 150 MHz but the calibration data is only available up to 60 MHz. Nonetheless, this step was necessary to understand the magnitude of the PA pressure pulse. The deconvolved pressure pulse was further converted to plane wave displacement pulse (Figure 6); its magnitude spectrum is shown in Figure 7. It clear that the generated PA pulse has a dominant response up to 20 MHz and the displacement generated up to 60 MHz are sufficient to be discernible on the displacement interferometer. However, the overall displacement magnitude of the PA pulse shown in Figure 6 extends to the non-linear performance region of the Michelson interferometer implemented at NPL. The phase shift, ø between the reference and the measurement optical beam is only linear for small displacements of up to 5 nm (Preston et al. 2003) although the actual limits remain to be properly quantified. The sub-fringe ultrasonic displacement imposes a linear limit which is fundamental to Michelson interferometers. Therefore the displacement pulse obtained using photoacoustic excitation although has required high frequency content its displacement magnitude however, is too high to be useful. Similar PA pulses were observed on a number of identical targets where the dominant response was in the frequency range of up to 30 MHz.

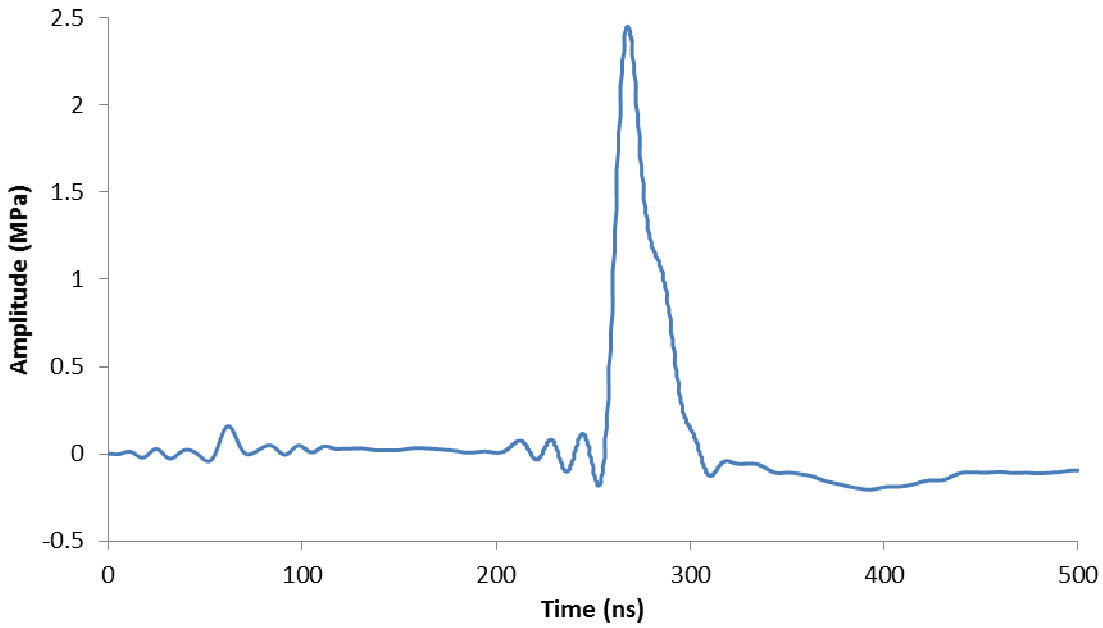

Figure 5 Deconvolved pressure pulse (IEC 62127-1 2013) of the hydrophone waveform shown in Figure 3 using magnitude and phase response up to 60 MHz.

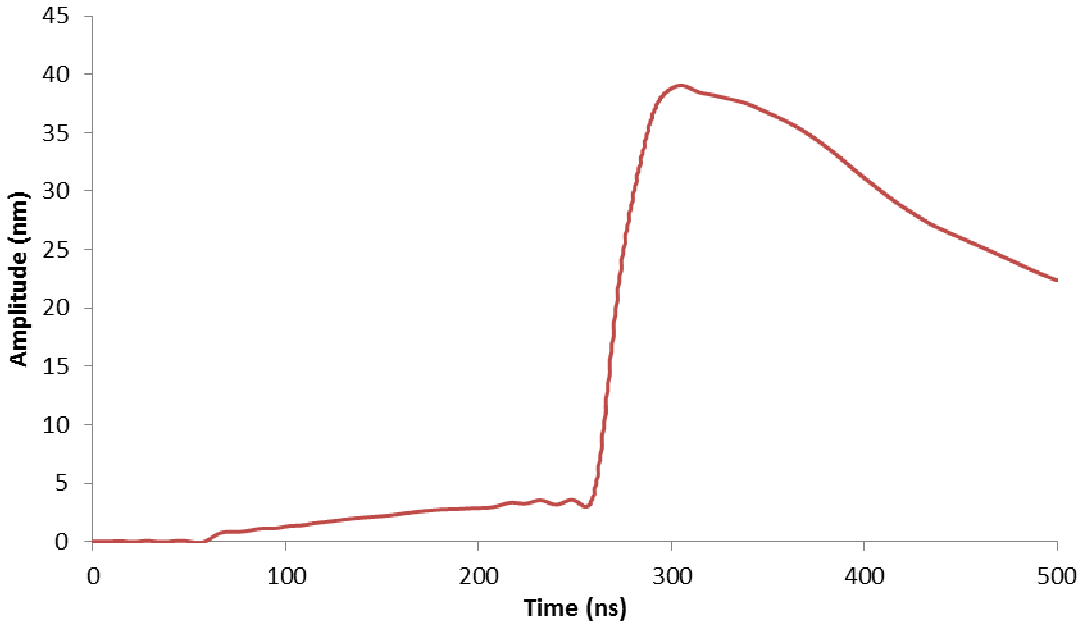

Figure 6 PA displacement pulse obtained by integrating the time-domain PA pressure pulse shown in Figure 5 and scaled by sound speed and density of water.

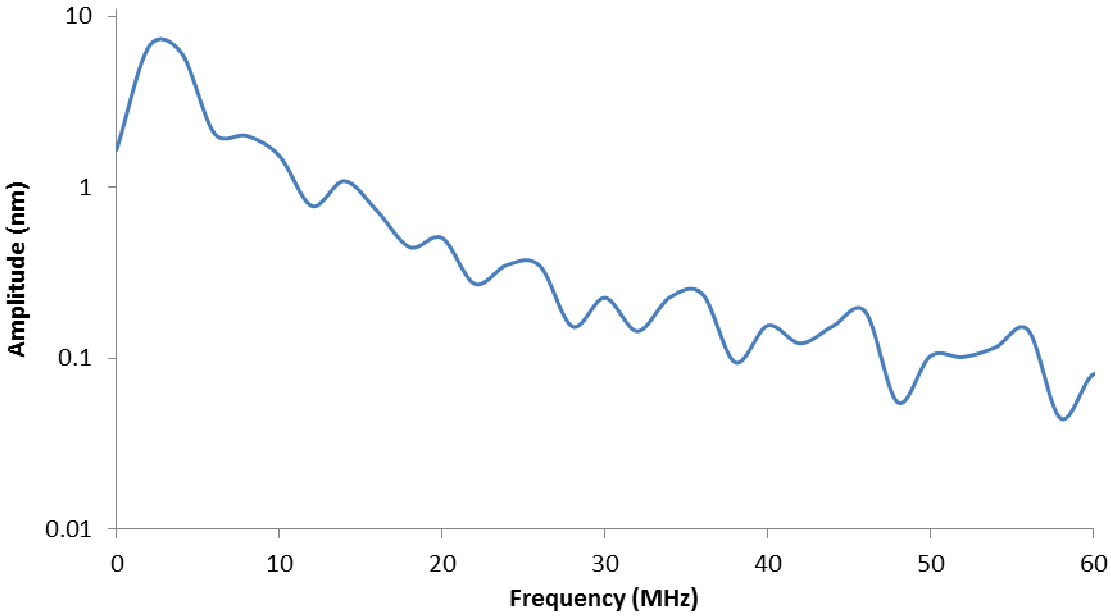

Figure 7 Magnitude spectrum of the displacement pulse shown in Figure 6.

The latest results are encouraging and they show that pressure and bandwidth in the right range can be generated. However, to obtain PA frequency components extending up to 100 MHz whose amplitude remains within the linear displacement region at all frequencies of interest will demand optimising the target and/or optical excitation scheme. The PA pulse shape obtained on NPL setup closely resembles the work of Hsieh et al. (2015); in their work the generated PA pulse pressure amplitudes were approximately 2 and 12 MPa with a dominant frequency response occupying a range of up to 30 MHz, pulse width was approximately 50 ns and the target thicknesses were approximately 25 and 58 µm. A

target whose absorption coefficient is sufficiently high such that it absorbs approximately 100 % of incident absorption within a very small depth (less than 20 µm) then the generated PA pulse shape and its magnitude response shape closely resembles that of the optical excitation pulse (Guo et al. 2011, Won Baac et al. 2010, Hou et al. 2007). Figure 6 is the normlaised magnitude response of the NPL's 6 ns laser pulse acquired from the scattered light using a high-speed photodetector of type DET08CL/M (Thorlabs, UK). It can be seen that the shape of the magnitude response has no pronounced low frequency features present in Figure 3. The effect on eventual displacement amplitudes is presently unknown which is of main interest but it suggests that target optimisation is crucial and could be a possible solution in restricting the amplitude levels of the generated PA pulse at low frequencies.

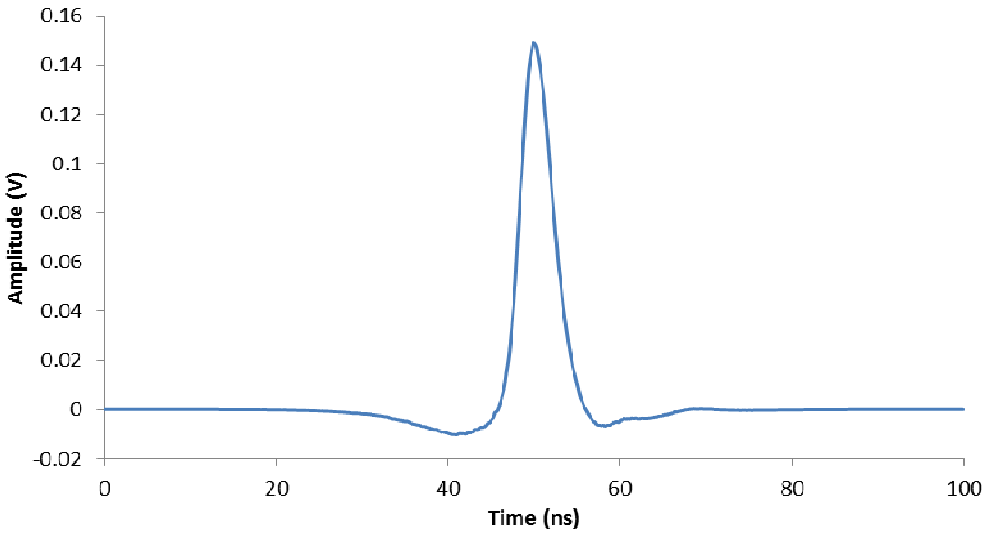

Figure 8 Laser pulse captured from scattered light in the experimental setup using high-speed photodetector of type DET08CL/M (Thorlabs, UK).

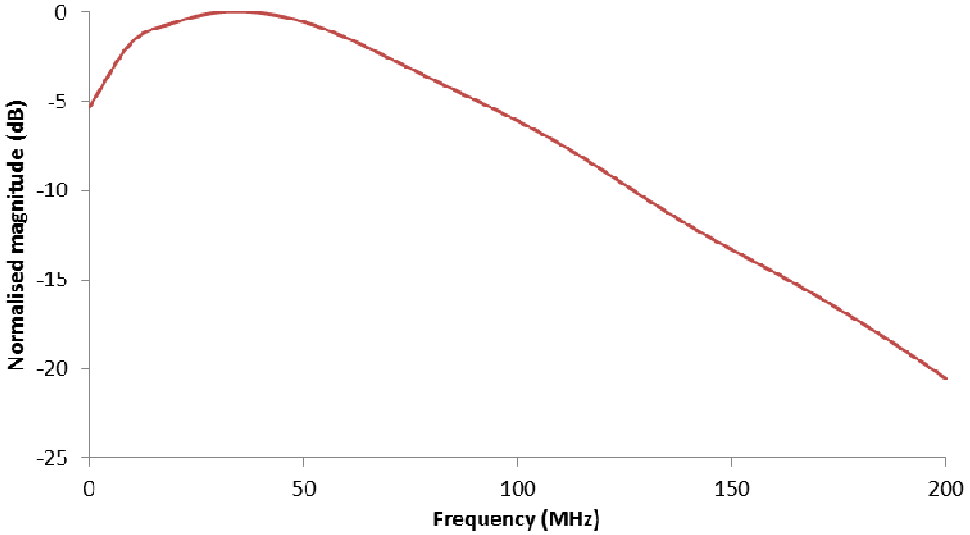

Figure 9 Normalised magnitude spectrum of the laser pulse shown in Figure 8.

Excitation schemes for improving the signal to noise of band-limited systems such as Chirp and Golay coding has long been employed for example in Radar, Medical Ultrasound Imaging, Sonar and Communications. In biomedical photoacoustics imaging and NDT, use of Chirped and Golay coded optical excitation is relatively new (Mienkina et al. 2010a, Mienkina et al. 2010b, Su and Li 2011, Zhang et al. 2012, Lashkari et al. 2015, Pierce et al. 2011). Although the laser at NPL is a single pulse system with a maximum repetition rate of 20 Hz, it still offers some flexibility for example each pulse can be divided in to a pulse train (Liu et al 2010). The individual pulse energy within a pulse train can be selectively attenuated to produce a pulse-train of arbitrary shape to excite the target. An optimisation involving target design and optical excitation scheme appears to be the way forward to limit the displacement amplitudes and yet maintain the broadband nature of the generated PA pulse.

5 SUMMARY

The literature review has revealed encouraging facts about this new area of science for NPL i.e. photoacoustics and its ability to generate high frequency and high pressure ultrasound suitable for calibrating hydrophones on NPL's primary standard displacement interferometer. In short, the generation of ultrasound using photoacoustic principles requires a time varying optical source which when illuminated on a target i.e. an optically absorbing material, converts the optical energy to propagating acoustic waves within the material. In order to efficiently convert optical energy to acoustic energy in the thermoelastic regime, the time varying optical source should satisfy the stress and thermal confinement times criteria of the target which are easily met when employing a pulsed laser of nanoseconds duration. The target should completely absorb the optical radiation within a small depth (ideally around 20 μm) and whose acoustic impedance is close to water for efficient coupling of ultrasound from the target to water. The target is usually a composite of optically absorbing particles (carbon and metallic nanoparticles) dispersed in an elastomeric polymer. The generation of high frequency and high pressure ultrasound requires optimisation of the composite material, its physical design, and the optical excitation scheme. The literature review section has a number of examples demonstrating these aspects and there appears to be potential for further optimisation which can be addressed within future work of NPL. Almost all researchers did not discuss a key requirement which is likely to be fundamental when carrying out experiments in metrology i.e. the stability of the target. It is clear that the applications discussed in the literature may not have demanded a stability criterion but for hydrophone calibrations on the primary standard it is essential. Therefore the targets developed at NPL must be subjected to rigorous systematic studies to determine for example the variation of PA pulse with optical pulse energy and repetition rate continuously over a few hours operation, longitudinal studies to check the performance or the shelf life of the target, the effect of water take-up by the target and the alteration of its chemical properties due to water absorption. Researchers who reported their findings in a quantitative manner i.e. using a hydrophone to quantify the high frequency

(> 60 MHz) and high pressure PA pulses seemed to clearly overlook the limited frequency calibration range of their hydrophones. Even if they did not, it is still not clear as to what measures they employed to quantify the characteristics of the PA pulse beyond the known frequency range. The effect of recovering the PA pressure pulse from the deconvolution process using the limited calibration frequency range of a hydrophone was demonstrated earlier in the report.

Within the current experimental PA setup implemented at NPL and for measurements carried out on simple targets made of spray coated black paint, the results suggest that the generated PA pulse amplitudes are at least 2.5 MPa. The measureable frequency range using a membrane hydrophone extends up to 150 MHz. The displacement PA pulse obtained by deconvolution using the limited calibration range of the hydrophone has a magnitude as high as 40 nm whilst its magnitude spectrum indicates a dominant low frequency response of 0.5 – 10 nm in the frequency range 0 – 20 MHz and thereafter it gradually decreases to about 0.1 nm at 60 MHz. It should be noted that the targets prepared were crude in nature, fabricated from a single material type and did not involve the systematic preparation required for more careful studies. The idea behind the use of spray paint targets was to evaluate the PA measurement setup and understand the systematics of the system. This process enabled us to develop useful knowledge of some aspects such as the characteristics of the PA pulse, its magnitude response and laser stability. A number of targets involving various elastomeric material types and filler particles are due to be prepared and tested within the current NMS project ending in Dec 2015 in collaboration with Photoacoustic Imaging group of UCL and Materials Division of NPL. Initially a number of targets prepared in a dip coated manner will be screened to shortlist those samples that produce optimal PA amplitudes. The shortlisted candidates will then be prepared in a controlled and consistent setup through the use of a spin coater where it is possible to control the thickness of the target layer which will help achieve desired optimisation.

It is clear that the PA pulse in its current form cannot be used naively on the interferometer to calibrate hydrophones as the generated PA displacement amplitudes extend to the nonlinear measurement region of the Michelson interferometer. The literature review points to a number of examples suggesting that it is possible to obtain PA pulses of varied shapes via target design and custom optical excitation. This should provide some optimisation capabilities to control the PA displacement amplitude and required high-frequency bandwidth i.e. up to 100 MHz which can only be explored to a limited extent within the current NMS project. Therefore continued research efforts will be essential beyond the current NMS programme extending over a period of at least three years to meet the desired objectives for which the photoacoustic is better placed compared to piezoelectric transducer technology, so as to meet the challenge for the future metrological requirements of ultrasound.

6 RECOMMENDATIONS

Through a detailed literature review and early experimental results obtained on NPL's photoacoustics measurement setup the following recommendations are made. These will advance the research in photoacoustics from a metrological perspective to support primary calibration of miniature medical hydrophones up to a frequency 100 MHz:

I. Develop in-house capability in conjunction with Materials Division of NPL with regards to the art and science of fabricating photoacoustic sources involving various polymer-filler combinations.

II. Conduct systematic investigations of photoacoustic sources for their suitability as alternate ultrasound sources with respect to their stability, damage threshold to optical energy, operational life, how they are affected by water and its effects on hydrophone calibrations.

III. Explore various possibilities of packaging the necessary illumination optics and the photoacoustic source for eventual application as a practical and safe source for not only primary standard hydrophone calibrations but also for secondary standards and characterisation of acoustic properties of materials such as speed of sound and attenuation.

IV. Investigate various target designs and optical excitation schemes i.e. pulse shaping, Chirp and Golay coded excitation to limit the photoacoustic displacement amplitude within the linear measurement range of the Michelson interferometer, yet still obtaining a broad bandwidth signal encompassing frequencies up to 100 MHz.

V. Increase modelling awareness and develop necessary mathematical models to support and underpin experimental observations and to guide experiments.

VI. Investigate methods to derive the nonlinear displacement corrections for primary standard Michelson interferometer.

VII. Extend NPL's hydrophone model developed for estimating the frequency response of standard bilaminar reference membrane hydrophones (GEC Marconi Ltd) to newer coplanar designs up to 100 MHz to co-validate photoacoustic modelling and interferometer calibrations.

7 REFERENCES

Aliev, A.E. et al., 2010. Thermal conductivity of multi-walled carbon nanotube sheets: radiation losses and quenching of phonon modes. Nanotechnology, 21(3), p.035709.

ArcScan 2015. Artemis3 Ultrasound Scanner Products and Technology. 2015. ArcScan: Artemis3 Ultrasound Scanner Products and Technology. [ONLINE] Available at: http://www.arcscan.com/products.php. [Accessed 22 June 2015].

Baac, H.W. et al., 2012. Carbon-nanotube optoacoustic lens for focused ultrasound generation and high-precision targeted therapy. Scientific reports, 2, p.989.

Bayer, C.L. et al., 2013. Photoacoustic signal amplification through plasmonic nanoparticle aggregation. J Biomed Opt, 18(1), p.16001.

Biagi, E. et al., 1997. Photoacoustic Generation: Optical Fiber Ultrasonic Destructive Evaluation and Clinical Diagnosis Sources for Non Destructive Evaluation and Clinical Diagnosis. Optical Review, 4(4), pp.481–483.

Biagi, E., Margheri, F. & Menichelli, D., 2001. Efficient laser-ultrasound generation by using heavily absorbing films as targets. IEEE Transactions on Ultrasonics, Ferroelectrics and Frequency Control, 48(6), pp.1669–1680.

Caddes, D.E., 1966. Conversion of Light to Sound by Electrostrictive Mixing in Solids. Applied Physics Letters, 8(12), p.309.

Chen, Y.-S. et al., 2011. Silica-coated gold nanorods as photoacoustic signal nanoamplifiers. Nano letters, 11(2), pp.348–54.

Cox, B. 2009. Modelling Photoacoustic Propagation in Tissue Using k-Space Techniques. In: Wang, L.V. ed. 2009. Photoacoustic Imaging and Spectroscopy, New York: CRC Press, pp.25-34.

Dehoux, T. et al., 2015. All-optical broadband ultrasonography of single cells. Scientific Reports, 5, p.8650.

DermaScan 2015. DermaScan skin ultrasound - Cortex Technology ApS. 2015. DermaScan skin ultrasound - Cortex Technology ApS. [ONLINE] Available at: http://www.cortex.dk/skin-analysis-products/dermascan-ultrasound.html. [Accessed 22 June 2015].

Diebold, G.J. 2009. Photoacoustic Monopole Radiation: Waves from Objects with Symmetry in One, Two, and Three Dimensions. In: Wang L.V. ed. 2009. Photoacoustic Imaging and Spectroscopy, New York: CRC Press, pp.25-34.

Duck, F.A. 1990. Physical Properties of Tissue: A Comprehensive Reference Book, London: Academic Press.

El-Brolossy, T. a. et al., 2008. Shape and size dependence of the surface plasmon resonance of gold nanoparticles studied by Photoacoustic technique. The European Physical Journal Special Topics, 153(1), pp.361–364.

Gopinath Minasamudram, R. et al., 2009. Thin film metal coated fiber optic hydrophone probe. Applied optics, 48(31), pp.G77–G82.

Guo, Y. et al., 2008. Sensitive molecular binding assay using a photonic crystal structure in total internal reflection. Optics express, 16(16), pp.11741–11749.

Han, Z. & Fina, A., 2011. Thermal conductivity of carbon nanotubes and their polymer nanocomposites: A review. Progress in Polymer Science (Oxford), 36(7), pp.914–944.

Hong, W.-T. & Tai, N.-H., 2008. Investigations on the thermal conductivity of composites reinforced with carbon nanotubes. Diamond and Related Materials, 17(7-10), pp.1577–1581.

Hsieh, B.-Y. et al., 2015. A laser ultrasound transducer using carbon nanofibers–polydimethylsiloxane composite thin film. Applied Physics Letters, 106(2), p.021902.

Huang, S.-W. et al., 2008. Low-noise wideband ultrasound detection using polymer microring resonators. , 92(19), pp.2006–2009.

Huke, P. et al., 2013. Novel trends in optical non-destructive testing methods. Journal of the European Optical Society, 8, pp.1–7.

Hurrell, A., 2004. Voltage to pressure conversion: are you getting `phased' by the problem? Journal of Physics: Conference Series, 1, pp.57–62.

Hwan Lee, S. et al., 2012. Reduced graphene oxide coated thin aluminum film as an optoacoustic transmitter for high pressure and high frequency ultrasound generation. Applied Physics Letters, 101(24), pp.2010–2014.

IEC 62127-1 2013. IEC 62127-1:2007+AMD1:2013. Ultrasonics - Hydrophones - Part 1: Measurement and characterization of medical ultrasonic fields up to 40 MHz, Edition 1.1, Geneva: IEC Publication.

IEC 62127-2 2013. IEC 62127-2:2007+AMD1:2013. Ultrasonics - Hydrophones - Part 2: Calibration for ultrasonic fields up to 40 MHz, Edition 1.1, Geneva: IEC Publication.

IEC 62359: 2010. Ultrasonics - Field characterization - Test methods for the determination of thermal and mechanical indices related to medical diagnostic ultrasonic fields, Edition 2 Geneva: IEC Publication.

Kim, P. et al., 2001. Thermal transport measurements of individual multiwalled nanotubes. Physical review letters, 87(21), p.215502.

Koch, C. & Molkenstruck, W., 1999. Primary calibration of hydrophones with extended frequency range 1 to 70 MHZ using optical interferometry. IEEE Transactions on Ultrasonics, Ferroelectrics, and Frequency Control, 46(5), pp.1303–1314.

Koch, C., 2003. Amplitude and phase calibration of hydrophones by heterodyne and time-gated time-delay spectrometry. IEEE Transactions on Ultrasonics, Ferroelectrics, and Frequency Control, 50(3), pp.344–348.

Koukoulas, T. et al., 2013. Primary ultrasonic interferometer photodiode characterization using frequency-modulated laser wavefront radiation. Metrologia, 50(6), pp.572–579.

Lashkari, B. et al., 2015. Simultaneous dual-wavelength photoacoustic radar imaging using waveform engineering with mismatched frequency modulated excitation. Optics Letters, 40(7), p.1145.

Leighton T. G. 1994. The Acoustic Bubble, London: Academic Press.

Li, Q. et al., 2009. Measuring the thermal conductivity of individual carbon nanotubes by the Raman shift method. Nanotechnology, 20(14), p.145702.

Link, S. & El-Sayed, M.A., 2000. Shape and size dependence of radiative, non-radiative and photothermal properties of gold nanocrystals. International Reviews in Physical Chemistry, 19(3), pp.409–453.

Liu, T. et al., 2010. Photoacoustic generation by multiple picosecond pulse excitation. Medical physics, 37(4), pp.1518–1521.

Lukes, J.R. & Zhong, H., 2007. Thermal Conductivity of Individual Single-Wall Carbon Nanotubes. Journal of Heat Transfer, 129(6), p.705.

Matsuda, Y., Yoshioka, M. & Uchida, T., 2014. Absolute Hydrophone Calibration to 40 MHz Using Ultrasonic Far-Field. MATERIALS TRANSACTIONS, 55(7), pp.1030–1033.

Maxwell, A. et al., 2008. Polymer Microring Resonators for High-Frequency Ultrasound Detection and Imaging. IEEE journal of selected topics in quantum electronics : a publication of the IEEE Lasers and Electro-optics Society, 14(1), pp.191–197.

Mienkina, M.P. et al., 2010a. Multispectral photoacoustic coded excitation imaging using unipolar orthogonal Golay codes. OPT EXPRESS, 18(9), pp.9076–87.

Mienkina, M.P. et al., 2010b. Experimental evaluation of photoacoustic coded excitation using unipolar golay codes. IEEE Transactions on Ultrasonics, Ferroelectrics, and Frequency Control, 57(7), pp.1583–1593.

Milas, S.M. et al., 2003. Acoustic characterization of microbubble dynamics in laser-induced optical breakdown. IEEE Transactions on Ultrasonics, Ferroelectrics, and Frequency Control, 50(5), pp.517–522.

Mizuno, K. et al., 2009. A black body absorber from vertically aligned single-walled carbon nanotubes. Proceedings of the National Academy of Sciences of the United States of America, 106(15), pp.6044–6047.

Moon, H. et al., 2015. Amplified Photoacoustic Performance and Enhanced Photothermal Stability of Reduced Graphene Oxide Coated Gold Nanorods for Sensitive Photoacoustic Imaging. ACS Nano, 9(3), pp.2711–2719.

Morris, P., Beard, P. & Hurrell, A., 2005. Development of a 50MHz optical fibre hydrophone for the characterisation of medical ultrasound fields. Proceedings - IEEE Ultrasonics Symposium, 3, pp.1747–1750.

Mosse, C. a. et al., 2014. Fiber optic ultrasound transducers with carbon/PDMS composite coatings. In A. A. Oraevsky & L. V. Wang, eds. Photons Plus Ultrasound: Imaging and Sensing 2014.

Paltauf, G. & Dyer, P.E., 2003. Photomechanical processes and effects in ablation. Chemical reviews, 103(2), pp.487–518.

Park, M.A., Lee, S.H. & Yoh, J.J., 2013. Characterization of laser-induced ultrasound signal by reduced graphene oxide thickness and laser intensity. Applied Physics B: Lasers and Optics, 113(3), pp.389–393.

Pierce, S.G. et al., 2011. Low peak-power laser ultrasonics. Nondestructive Testing and Evaluation, 26(3-4), pp.281–301.

Preston, R.C. et al., 2003. Primary calibration of membrane hydrophones in the frequency range 0.5 MHz to 60 MHz. Metrologia, 36(4), pp.331–343.

Robinson, S.P., Bacon, D.R. & Moss, B.C., 1990. The measurement of the frequency response of a photodiode and amplifier using an opto-mechanical frequency response calibrator. Measurement Science and Technology, 1(11), pp.1184–1187.

Sazbo, T. 2014. Diagnostic Ultrasound Imaging: Inside Out, 2nd Edition, Academic Press.

Scruby, C.B., and Drain, L.E. 1990. Laser Ultrasonics: Techniques and Applications, Bristol: Adam Hilger.

Smith, R. A. & Bacon, D.R., 1990. A multiple-frequency hydrophone calibration technique. The Journal of the Acoustical Society of America, 87(5), pp.2231–2243.

Spitalsky, Z. et al., 2010. Carbon nanotube-polymer composites: Chemistry, processing, mechanical and electrical properties. Progress in Polymer Science (Oxford), 35(3), pp.357–401.

Su, S.-Y. & Li, P.-C., 2011. Coded excitation for photoacoustic imaging using a high-speed diode laser. Optics express, 19(2), pp.1174–1182.

Sun, K. et al., 2011. Simulation on photoacoustic conversion efficiency of optical fiber-based ultrasound generator using different absorbing materials. In W. Ecke, K. J. Peters, & T. E. Matikas, eds. Smart Sensor Phenomena, Technology, Networks and Systems. International Society for Optics and Photonics, pp. 798213–1–7.

Theocharous, E. et al., 2014. The partial space qualification of a vertically aligned carbon nanotube coating on aluminium substrates for EO applications. Optics express, 22(6), pp.7290–307.

Tian, Y. et al., 2013. Fiber-optic ultrasound generator using periodic gold nanopores fabricated by a focused ion beam. Optical Engineering, 52(6), p.065005.

Vannacci, E. et al., 2014. Miniaturized fiber-optic ultrasound probes for endoscopic tissue analysis by micro-opto-mechanical technology. Biomedical microdevices, 16(3), pp.415–26.

Verweij, M.D. et al. 2014. Simulation of Ultrasound Fields. In: Brahme, A. ed. 2014. Comprehensive Biomedical Physics, 1st Edition, Elsevier Science Ltd, pp. 465-500.

VisualSonics 2015: High-Resolution Imaging. 2015. MicroScan™ Transducers | Real-time, in vivo imaging systems for pre-clinical research - VisualSonics : High-Resolution Imaging. [ONLINE] Available at: http://www.visualsonics.com/products/vevo-2100/ms-transducers. [Accessed 22 June 2015].

Wang L.V. ed. 2009. Photoacoustic Imaging and Spectroscopy, New York: CRC Press.

Wang, Z., Ha, S. & Kim, K., 2012. Evaluation of finite element based simulation model of photoacoustics in biological tissues. In J. G. Bosch & M. M. Doyley, eds. Proc. SPIE. p. 83201L–83201L–9.

Won Baac, H. et al., 2010. Carbon nanotube composite optoacoustic transmitters for strong and high frequency ultrasound generation. Applied physics letters, 97(23), p.234104.

Wu, N. et al., 2010. Theoretical analysis of a novel ultrasound generator on an optical fiber tip. Fiber Optic Sensors and Application VII, 7677, p.76770X–76770X–7.

Zhang, H. et al., 2012. Simultaneous multispectral coded excitation for photoacoustic imaging. IEEE International Ultrasonics Symposium, IUS, pp.1402–1405.

Zou, X. et al., 2013. Polydimethylsiloxane thin film characterization using all-optical photoacoustic mechanism. Applied optics, 52(25), pp.6239–44.

Zou, X. et al., 2014. Broadband miniature fiber optic ultrasound generator. Optics express, 22(15), pp.18119–27.